Physica Scripta

PAPER

Velocity selective multiple two-photon dark and bright resonances in Potassium vapor

RECEIVED
30 April 2024

REVISED
21 June 2024

ACCEPTED FOR PUBLICATION
24 June 2024

PUBLISHED
3 July 2024

Gourab Pal[1], **Subhasish Dutta Gupta**[2,3,4] **and Saptarishi Chaudhuri**[1]

[1] Raman Research Institute, Bangalore, India
[2] TIFR Hyderabad, India
[3] IISER Kolkata, India
[4] IIT Jodhpur, India

E-mail: gourab@rrimail.rri.res.in

Keywords: Electromagnetically induced transparency, Electromagnetically enhanced absorption, Doppler broadening, adiabatic elimination, swappable transition pathway, quantum optics, atom-light interaction

Abstract

We report the observation of two additional sub-natural line width quantum interferences in the D_2 manifold of ^{39}K vapor, in addition to the usual single Electromagnetically Induced Transparency (EIT) peak. In a typical three level Λ-type system, only one EIT peak is observed. However, here we report observation of two additional line shapes riding on top of the absorption profile. The fact that the hyperfine splitting is smaller than the Doppler width in ^{39}K allows the probe and control beams to swap their transition pathways in different velocity groups of atoms even when their frequencies are kept constant. Our observations are in striking contrast to standard EIT measurements. These findings are in quantitative agreement with density matrix formalism taking into account velocity-selective two-photon resonances. Owing to the favorably low ground hyperfine splitting (Δ_{hf}) in ^{39}K, which allows a significantly large number of atoms with a Doppler shift greater than or equal to the Δ_{hf}, the strength of these additional resonances is strong compared to that of other alkali atoms such as ^{87}Rb, ^{133}Cs where these resonances can not be observed. The control photon detuning to atomic transition captures the nature of the coherence; therefore an unusual phenomenon of conversion from perfect transparency to enhanced absorption of the probe photon is observed and explained by utilizing the adiabatic elimination of the excited state in the Master equation. Controlling such dark and bright resonances leads to new applications in quantum technologies such as frequency-offset laser stabilization and long-lived quantum memory.

1. Introduction

For the past few decades, manipulating and controlling the optical responses [1] of atomic media using quantum interference across excitation channels has been a versatile field of study. One of the most fascinating quantum interference phenomena is electromagnetically-induced transparency (EIT) [2, 3], which dramatically modifies the responses of the medium and opens the door to several cutting-edge applications in quantum information processing [4], including the creation of high-precision quantum sensors [5], atomic clocks [6], and magnetometers [7]. As an application to quantum memory [8], it is feasible to slow down [9] or store photons [10] for a considerable amount of time because of the steep anomalous dispersion in an EIT medium. The EIT medium can be used to enhance the self-Kerr effect [11], creating entangled bi-photons[12] with application in quantum communication. More recently, exotic effects such as Goos-Hänchen [13], and Imbert-Fedorov shifts [14] have been observed using EIT medium.

Numerous experiments have been carried out in diverse atomic systems such as ^{87}Rb [15], ^{133}Cs [16, 17], ^{23}Na [18], metastable He [19, 20], molecular Lithium [21] and EIT with Rydberg atoms [22, 23]. These systems exhibit strong quantum interference phenomena (EIT or Electromagnetically Induced Absorption—EIA) owing to their wide ground state separation and considerable energy spacing among excited states. Furthermore,

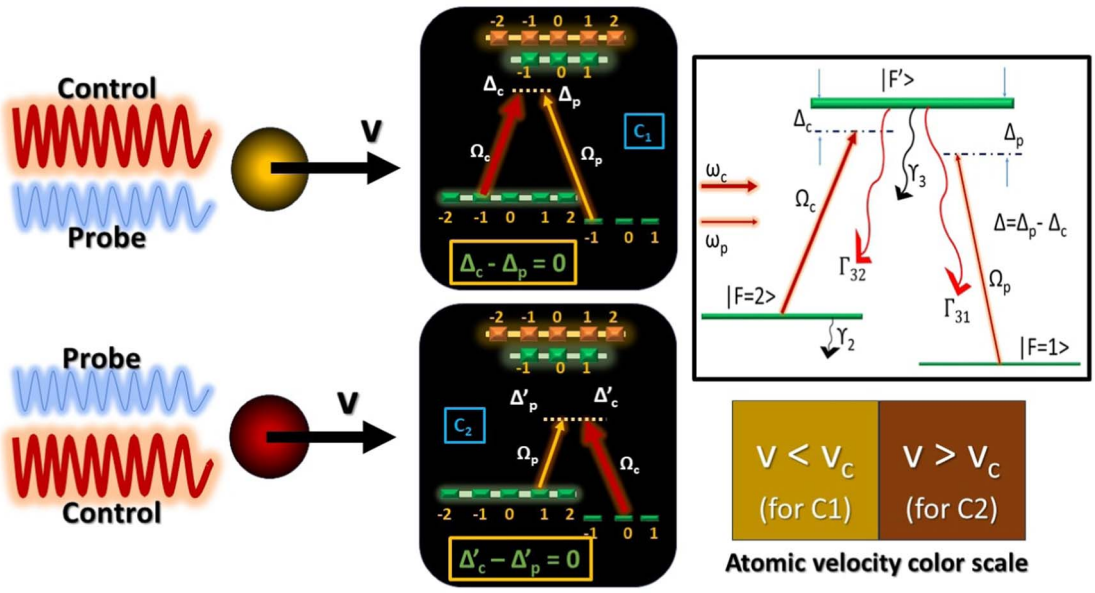

Figure 1. Swapping of excitation pathways of control and probe beam depending on the critical velocity $v_c = \frac{2\pi \times 461.7}{k}$ of the atoms. See text for more details. (Inset) Representative three-level Λ system. $|F = 1\rangle$, $|F = 2\rangle$ are ground and metastable state whereas $|F'\rangle$ is considered as unresolved excited state. Δ_p, Δ_c and Δ are single photon detuning of probe, single photon detuning of control and two-photon detuning, respectively. Γ_{32}, Γ_{31} are spontaneous decays of excited state $|F' = 3\rangle$ to $|F = 2\rangle$ and $|F = 1\rangle$ in presence of Doppler broadening respectively. γ_3 and γ_2 are the energy conserving dephasing of states $|F' = 3\rangle$ and $|F = 2\rangle$ respectively. $\omega_c, \omega_p, \Omega_c, \Omega_p$ are angular frequencies and Rabi frequencies for control and probe beam, respectively. The colour map in bottom-right indicates the velocity group of atoms responsible for creating line shapes C_1 and C_2. This colour codes map to the false color of the atoms in the same diagram.

in a typical atomic vapor, the Doppler broadening is much smaller than the ground state separation, leading to the observation of only one EIT or EIA feature in a given experimental configuration. On the other hand, the ground state separation in ^{39}K is smaller (461.7MHz [24]) than the Doppler broadening at room temperature which makes the study of EIT in ^{39}K intriguing.

There exist very few quantum interference-based experiments in ^{39}K, Long *et al* [25] used a chirped waveform electro-optic modulator to investigate the EIT, A Sargsyan *et al* [26] demonstrated on-resonance EIT and Gozzini *et al* [27] observed EIT-EIA transition in Hanle configuration with polarization as a tuning parameter. In this article, we experimentally demonstrate the emergence of three distinct quantum interference line shapes in a Λ-type system in ^{39}K atomic ensemble. These observations are in sharp contrast to the typical EIT-EIA measurements in other alkali vapors such as Rb, and Cs. The EIT-EIA can be physically understood following the two-photon resonance phenomenon and we can completely observe the two-photon resonance in the Rb or Cs atoms in the Λ-configuration as well. However, what is unique to ^{39}K is that the ground state hyperfine splitting is smaller than the Doppler broadening at investigation temperature. This allows for a fortuitous swapping of the transition pathways as will be shown in details in the following sections, which in turn is responsible for observing additional quantum interference signals reported in this article. We note that such swapping of the transition pathways is generally allowed in all physical systems where EIT-EIA phenomena is experimentally observed including well studied atomic systems such as Rb [28–30] and Cs [17]. Consequently, a group of atoms having velocity exceeding a critical velocity $v_c = \frac{2\pi\Delta_{hf}}{k}$, (where $\Delta_{hf} = 461.7$ MHz is the ground state hyperfine splitting, k is the wave vector) can create another two-photon resonance by interchanging the excitation pathways of probe and control beams as depicted in the figure 1.

Another two-photon resonance is observed when both the control and probe beam share a common ground state, and this line shape carries a contribution from the swapping configuration. The underlying criteria for satisfying the two-photon resonance condition need not be tied to the identification of the control and pump beam. As shown in figure 1, a laser light connecting $F = 1$ to F' can equally be considered as a probe or control. However, this interchange of labels can not be satisfied ubiquitously. Potassium atoms offer an interesting scenario where this label exchange is supported because of the fact that the Doppler broadening is of the same order as Δ_{hf}. Our results reported in this article are critically dependent on this fact. More details are described in the theory section. This atom-assisted swapping is indeed unique to Potassium because the two Doppler absorption profiles are accessible to both the control and the probe beam, thus making this swap possible. On the other hand, in the case of ^{87}Rb or ^{133}Cs, the critical velocity lies much outside (typically Δ_{hf} is one order of

magnitude higher compared to Doppler broadening) the Maxwell-Boltzmann velocity distribution, hence this velocity selective multiple resonances are never observed. Usually, only one line shape in a given probe-control configuration is observed in those experiments. Apart from observing these additional resonances, we also observe a transition from complete transparency to enhanced absorption as we vary the control beam detuning from the blue side to the red side of atomic resonance. However, the two-photon resonance condition is always satisfied to observe all the resonances. Accessing different types of dark and bright quantum resonances by detuning as a tuning knob will help set up frequency references for lasers operating at points very far from atomic reference lines. This technique is also useful for storage and retrieval of light far off-resonant with respect to atomic transitions.

The article is structured as follows. A detailed density matrix-based theory that is required to understand these additional line shape observations is presented in section 2. Section 3 presents the experimental details. We discuss important results and interpretations in section 4. Finally, in section 5, we extend the possible applications of the results.

2. Theoretical concepts

A semi-classical approach with density matrix formalism is applied to this three-level Λ system as shown in the inset of figure 1. The two ground states are $|F=1\rangle$ and $|F=2\rangle$ hyperfine levels in $5^2S_{1/2}$ and the excited state $|F'=3\rangle$ is considered as unresolved $|F'\rangle$ in $5^2P_{3/2}$ containing F' = 1 and 2 states. A control beam connects levels $|F=2\rangle$ and $|F'\rangle$ whereas the probe beam connects levels $|F=1\rangle$ and $|F'\rangle$. The von-Neumann equation governing the dynamics of a mixed state is $\dot{\rho}=-\frac{i}{\hbar}[H,\ \rho]$. Here ρ is the density matrix of the system, and H is the EIT Hamiltonian [1] given by

$$H=-\frac{i}{\hbar}\begin{bmatrix}0 & 0 & \Omega_p\\ 0 & 2(\Delta_p-\Delta_c) & \Omega_c\\ \Omega_p & \Omega_c & 2\Delta_p\end{bmatrix} \tag{1}$$

However, there are many decay processes such as spontaneous emission, dephasing, or decoherence due to inhomogeneous magnetic fields, ground state collisions, and spin-exchange collisions. Such terms make the above Hamiltonian non-unitary. We can use a Lindblad term [31], which needs to be added to the above Hamiltonian to correctly describe our present system. The Lindbladian approach in quantum Master equation (QME) is beneficial here as we are restricting our calculations to three-level systems with considerable energy separations. However, the complex multi-level systems with strong decoherence rates, can be solved using exact numerical methods [32, 33] where approximations such as weak coupling, Born-Markovian approximation or secular approximations may not be valid. For simpler description, we assume the validity of QME [15, 34, 35] in our system which qualitatively and quantitatively supports our findings as discussed in the results section. The dominant decay processes are due to Doppler-broadened spontaneous emission and energy-conserving dephasing effects, such as the collision of atoms with walls, and atom-atom collisions. The non-unitary Lindbladian term is given by

$$\mathcal{L}\rho=\Gamma_{31}\mathcal{D}[\hat{\sigma}_{1,3}]\rho+\Gamma_{32}\mathcal{D}[\hat{\sigma}_{2,3}]\rho+\gamma_2\mathcal{D}[\hat{\sigma}_{2,2}]\rho+\gamma_3\mathcal{D}[\hat{\sigma}_{3,3}]\rho \tag{2}$$

where Γ_{ij} denotes spontaneous decay rate from state i to state j, γ_i is an energy-conserving dephasing term for state i, $\hat{\sigma}_{i,j}$ is a jump operator defined as $\hat{\sigma}_{i,j}=|i\rangle\langle j|$ and $\mathcal{D}$ is coined as Lindblad super-operator whose action is defined as $\mathcal{D}[A]B=ABA^\dagger-\frac{1}{2}\{A^\dagger A,\ B\}$ for any two operators A and B. In our case, state $|1\rangle(|2\rangle)$ is identified as $5S_{1/2}|F=1\rangle$ ($5S_{1/2}|F=2\rangle$) and state $|3\rangle$ is $5P_{3/2}|F'\rangle$. Upon simplification, $\mathcal{L}\rho$ reduces to

$$\mathcal{L}\rho=-\frac{1}{2}\begin{bmatrix}0 & \gamma_2\rho_{12} & \Gamma_3\rho_{13}\\ \gamma_2\rho_{12}^* & 0 & (\Gamma_{31}+\Gamma_{32}+\gamma_3+\gamma_2)\rho_{23}\\ \Gamma_3\rho_{13}^* & (\Gamma_{31}+\Gamma_{32}+\gamma_3+\gamma_2)\rho_{23}^* & 0\end{bmatrix} \tag{3}$$

Here $\Gamma_3=\Gamma_{32}+\Gamma_{31}+\gamma_3$ is the total decoherence of the excited state, γ_2 indicates the ground state decoherence, γ_3 is the excited state energy conserving decoherence. Under steady-state conditions, the required coherence can be solved as follows -

$$\dot{\rho}_{12}=\left[-\frac{1}{2}\gamma_2+i(\Delta_c-\Delta_p)\right]\rho_{12}-i\frac{\Omega_c}{2}\rho_{13}+i\frac{\Omega_p}{2}\rho_{32}=0 \tag{4}$$

$$\dot{\rho}_{13}=\left[-\frac{1}{2}\Gamma_3-i\Delta_p\right]\rho_{13}-i\frac{\Omega_c}{2}\rho_{12}-i\frac{\Omega_p}{2}=0 \tag{5}$$

After solving the above two coupled linear equations and applying rigorous algebra, the susceptibility seen by the probe $\chi(\omega_p)$ can be obtained by the solving coherence terms under steady-state conditions as -

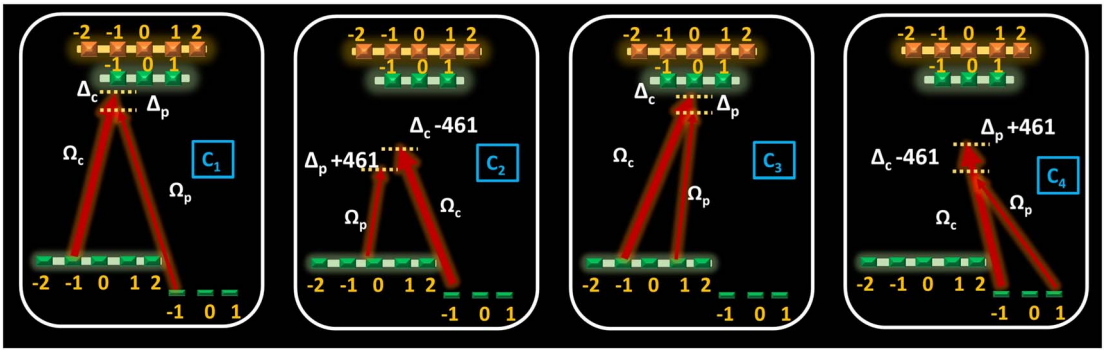

Figure 2. All four Λ-type configurations are supported due to small ground state splitting (see text) in ^{39}K atomic ensemble. Here ground states are $|F=1\rangle$ (indicated by a thin line) and $|F=2\rangle$ (indicated by a relatively thick line).

$$\chi_p(\Delta_p,\,\Delta_c) = \frac{2n|d_{13}|}{\epsilon_0 E_p}\frac{\Omega_p[2i\Delta+\gamma_2]}{-4i\Delta_p\Delta + i\Omega_c^2 - 2\Delta_p\gamma_2 + i\Gamma_3[2i\Delta+\gamma_2]} \tag{6}$$

Here, n is the density of atoms at cell temperature T, $|d_{13}|$ is the dipole matrix element, E_p is the probe field amplitude, Ω_p, Ω_c are the probe and control Rabi flopping frequencies, respectively and Δ_p, Δ_c and $\Delta = \Delta_p - \Delta_c$, are the respective probe detuning, control detuning, and two-photon detuning from a given transition (see inset of figure 1).

The imaginary part of equation (6) reliably represents the probe absorption, as described in the scenario in configuration C_1 of figure 2, creating a transparency window at two-photon resonance $\Delta = 0$. However, in the case of ^{39}K, two additional quantum resonances are observed as we keep scanning the probe beam frequency. The ground state hyperfine splitting of Potassium atoms is 461.7 MHz which is smaller than the unresolved (there are two Doppler absorptions that overlap in the case of Potassium) Doppler broadened absorption profile (~684 MHz at temperature 60°C).

Using the relation $\delta_D = k.\,v$, where δ_D is the detuning due to the Doppler effect, k is the beam's wavevector and v is the velocity of atoms, we can calculate the group of atoms that can account for this δ_D which turns out to be at least 353 m/s. This is called the critical velocity v_c which is the minimum velocity component along the beam propagation direction for atom-assisted swapping. Interestingly, this value is close to the most probable velocity at this temperature; therefore, a significant number of atoms can help this swapping by overcoming the 461.7 MHz ground state hyperfine splitting. This means that we can expect another lambda system to satisfy the two-photon resonance condition when the excitation pathways of the probe and control beam are interchanged (461.7 MHz separation) across the two overlapping Doppler profiles. Atoms with velocity components 353 m/s or more along the direction of beam propagation can now support this swapping through the Doppler effect. This type of atom-assisted swapping of excitation pathways can only be observed in ^{39}K atoms, because there is a good number of atoms at this detuning. On the other hand, in the case of say ^{87}Rb, the atom-assisted swapping is not observable as there exist almost no atoms in the Maxwell-Boltzmann distribution that can overcome the ground state splitting of $\Delta_{hf} = 6.8$ GHz with a corresponding critical velocity $v_c = 5304$m/s.

The swapping mechanism can be explained as follows. Let us say that prime ($'$) denotes the swapped frame. Before swapping, $\Delta_c = \Delta_p$ and hence $\Delta = 0$ that yields a quantum resonance line shape (C_1). After atom-assisted swapping of the excitation pathways, the control beam now connects levels $|F=1\rangle$ and $|F'\rangle$ (since the control beam frequency will be kept fixed during the experiment while probe frequency will be scanning across the whole D_2 manifold), so the control detuning becomes $\Delta_c \rightarrow \Delta_c' = \Delta_c - 461.7$. Because the probe beam now connects levels $|F=2\rangle$ and $|F'\rangle$, the probe detuning becomes $\Delta_p \rightarrow \Delta_p' = \Delta_p + 461.7$. However, the probe beam is scanning for all possible frequencies, hence, Δ_p' will adjust its value such that two-photon resonance is obtained. Let us denote variable probe detuning as $\tilde{\Delta}_p' = \Delta_p' \pm \delta$ with δ is the detuning adjustment parameter to satisfy the two-photon resonance. Therefore, $\Delta_p' = \Delta_p \pm \delta + 461.7$, irrespective of the sign of δ which can be either positive or negative. Therefore in this swapped frame, the two-photon resonance can be written as

$$\Delta' = \Delta_p' - \Delta_c' = (\Delta_p \pm \delta + 461.7) - (\Delta_c - 461.7) = \pm\delta + 923.4 \tag{7}$$

The atoms eventually adjust δ to satisfy two-photon resonance condition which is schematically described in Configuration C_2. The other two configurations C_3 and C_4 rely on the same principle, the only difference is that both beams have a common ground state either $|F=1\rangle$ or $|F=2\rangle$ and collectively appears in the middle of the above two features. Finally, the overall probe absorption profile is obtained by adding the contributions from all

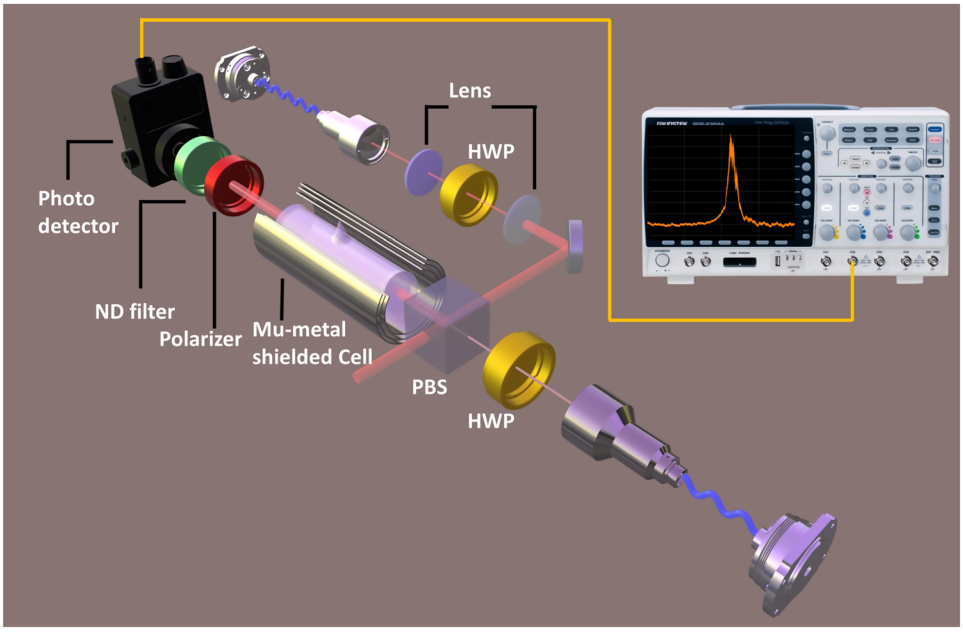

Figure 3. Schematic of experimental setup. Essential optical components are labeled in the figure.

four configurations and averaged over velocities using a 1D Maxwell-Boltzmann velocity distribution

$$\alpha_p = \sum_{i=1}^{4} C_i \int_{v=-\infty}^{+v=\infty} Im(\chi)_i \mathcal{P}(v)\, dv \tag{8}$$

Here i is for case C_i and $\mathcal{P}$ is the 1D Maxwell-Boltzmann velocity distribution given by

$$\mathcal{P} = \frac{1}{\sqrt{2\pi}\, D} e^{-\frac{v^2}{D^2}} \tag{9}$$

where $D = \sqrt{\frac{2k_B T}{m}}$ is the most probable velocity.

3. Experimental details

Figure 3 shows the schematic of the experiment. Two independent grating stabilized diode lasers (Toptica DL Pro and DL100) are used as control and probe beams. The probe and control lasers are tuned near $F = 1$ to F' and $F = 2$ to F' respectively in the D_2 manifold of ^{39}K, with a typical laser line width of 1 MHz. Two separate acousto-optic modulators are used to independently control the intensity and detuning of the probe and the control beams. The frequency reference is obtained using saturated absorption spectroscopy as shown in figure 4 (right). A 75 mm long and 25 mm diameter spectroscopy-grade commercial vapor cell containing ^{39}K (in natural abundance, ~93%) is placed inside a three-layered μ-metal jacket to efficiently shield any stray magnetic field.

The μ-metal shielding along with two μ-metal caps (to block stray fields from the sides), effectively blocks the external stray magnetic field down to 10mG level. This is measured using a Gauss-meter probe. In presence of such small magnetic field, we can assume the m_F states as practically degenerate for our current description. From a mathematical point of view, the frequency separation of two m_F states on application of magnetic field B can be written as

$$\nu = \frac{\mu_B}{h}(g_F B) \tag{10}$$

A small calculation yields the splitting rate 1.4 MHz/Gauss. So, for 10mG, the splitting will be around 10's of kHz which is not significant as compared to 3-4 MHz line-widths measured in our experiment. Hence, we can safely ignore the residual magnetic field effect and assume the magnetic sub-levels as near degenerate.

The probe and control beams are mode-filtered using single mode polarization maintaining fibers and passed through two independent telescopic arrangements with exit beam diameters of 1 mm and 4 mm, respectively. The two beams are prepared in orthogonal linear polarization (lin $\perp$lin) states and merged using a polarizing beam splitter cube before being transmitted to the atoms. The probe laser is kept in the frequency scan

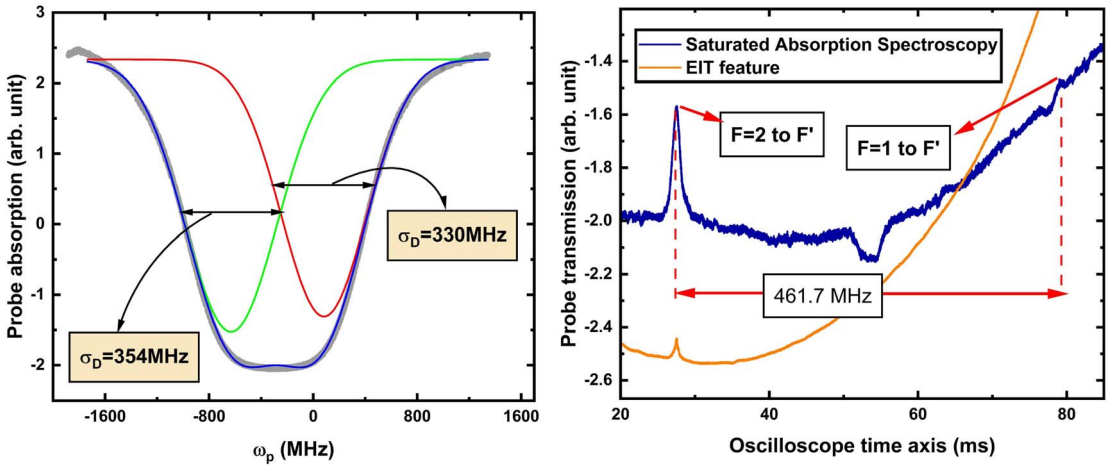

Figure 4. (Left) Representation of overlapping Doppler broadened absorption profiles. The thick grey line is the experimental data, and the red and green are individual Doppler absorption fitted by Gaussian and the blue line is the convolution of two Doppler. (Right) Saturated Absorption Spectroscopy of ^{39}K was used for the conversion of time scales in the oscilloscope to frequency scales.

mode whereas the control laser frequency is maintained at various detunings. Finally, the control beam is filtered out using a linear polarizer (extinction ratio 1: 10^5), and the signal is obtained using a photo-detector (Thorlabs PDA10A2) with 150 MHz bandwidth. A high-speed oscilloscope (2Gs/sec) is used for visualization and data recording.

The ground state hyperfine splitting is 461.7 MHz. At 333 K, the overlapping Doppler width is 684 MHz, calculated using the formula $\sigma_D = \sqrt{\frac{k_B T}{mc^2}}\,\omega_p$ [36], where k_B is the Boltzmann constant, m is the atomic mass, c is the velocity of light and ω_p is the probe frequency in Hz. Figure 4(left) shows the convolution of two Doppler broadened absorptions for $|F=1\rangle \rightarrow |F'\rangle$ and $|F=2\rangle \rightarrow |F'\rangle$. For theoretical modeling, we have taken the Doppler decoherence $\gamma_3 = 342$ MHz along with the total spontaneous decay of the excited state $\Gamma_3 = \Gamma_{32} + \Gamma_{31} = 684$ MHz when dealing with line shapes inside any of the Doppler.

Doppler-free Saturated Absorption Spectroscopy is performed using an independent vapor cell. The blue line in figure 4 (right) represents the hyperfine transition lines where the strongest peak corresponds to $|F=2\rangle \rightarrow |F'\rangle$ transition, the weakest peak corresponds to $|F=1\rangle \rightarrow |F'\rangle$ transition and the middle dip is the crossover resonance in the spectroscopy of ^{39}K. The orange line shows the typical dark resonance. The separation between the two peaks in the spectrum refers to the ground hyperfine splitting as

$$|T_{|F=2\rangle\rightarrow|F'\rangle} - T_{|F=1\rangle\rightarrow|F'\rangle}| = 461.7\text{MHz} \tag{11}$$

From the above equation, all time scales from the oscilloscopes can be converted to frequency scales.

4. Results and discussions

The ground state splitting of the Potassium atom is 461.7 MHz which is smaller than the unresolved two Doppler broadened absorption profiles (684 MHz at a cell temperature of 60 °C). Under these circumstance, the usual EIT peak with $\Delta = 0$ is observed, which corresponds to the standard configuration C_1 in figure 1. However, the excitation pathways of the control and probe beams can be swapped by atoms as described in the theory section. The swapping mechanism is illustrated in figure 1 where, as an example, $\Delta_c = -923.4$ MHz is taken. Before swapping, $\Delta_c = \Delta_p = -923.4$ MHz, the two-photon detuning is satisfied. However after swapping, $\Delta_c' = \Delta_c - 461.7 = -1385.1$ and $\Delta_p' = \Delta_p + 461.7 = -461.7$. Since the probe laser is scanning, the probe frequency is adjusted by setting $\delta = -923.4$ MHz, so that $\Delta_p' = -1385.1$ and the two-photon detuning condition is satisfied in this swapped frame. A third line shape is obtained by applying the same arguments but with control and probe beam making a valid Λ from the same hyperfine state either $|2\rangle$ (for the case C_3) or $|1\rangle$ (for the case C_4). See figure 2 for all four possible configurations. The table 1 shows few of the detuning values for C_1 and C_2 configurations. In this table, $\tilde{\Delta'}_p$ is the adjusted probe detuning in the swapped frame. The probe beam always adjust −923.4 MHz to get this two-photon resonance. Apart from having four different cases as shown in figure 2, there are multiple Λ systems possible within a given case owing to the existence of near-degenerate magnetic sub-levels of each hyperfine state. Considering the configuration of case C_1, a few Λ's are shown in figure 5 where we use blue lines for linearly polarized light and red lines for circularly polarized light. Because we use linear polarization in our experiment, and a linear polarization state is a

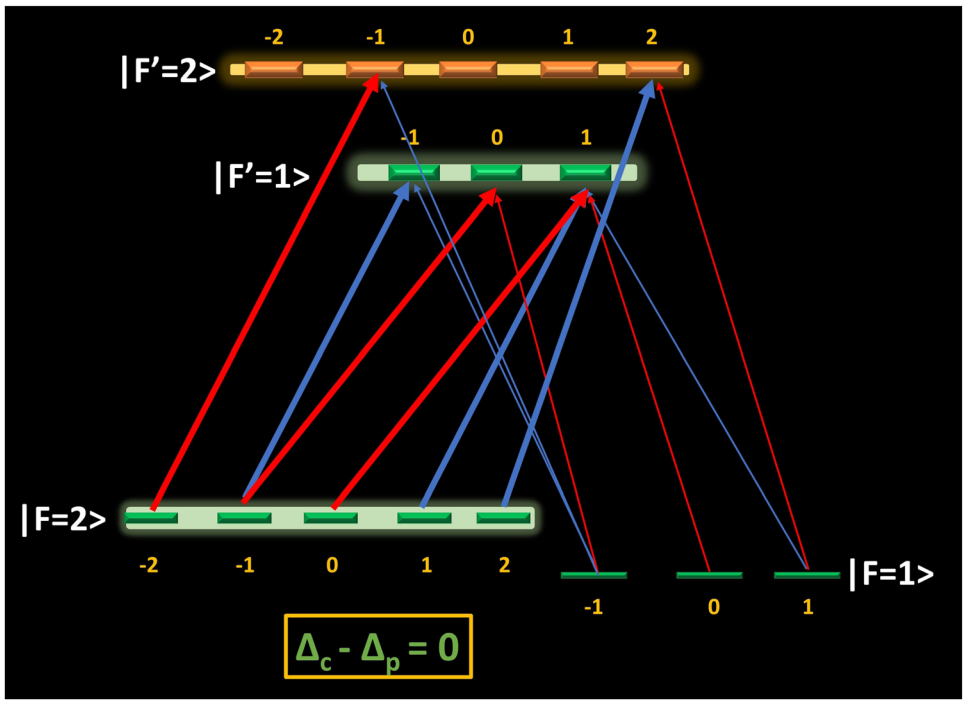

Figure 5. Demonstration of multiple Λ systems for two types of polarization of light. Blue lines are used for π polarized light and red lines are used for σ polarized light. Only a few $\Lambda's$ are shown here for clarity.

Table 1. Table of data in MHz unit for different detuning before and after swapping.

$C_1\,(\nu < \nu_c)$			$C_2\,(\nu > \nu_c)$				
MHz unit			MHz unit				
Δ_p	Δ_c	Δ	Δ'_p	Δ'_c	δ	$\tilde{\Delta}'_p$	Δ'
−923.4	−923.4	0	−461.7	−1385.1	−923.4	−1385.1	0
−461.7	−461.7	0	0	−923.4	−923.4	−923.4	0
0	0	0	461.7	−461.7	−923.4	−461.7	0
461.7	461.7	0	923.4	0	−923.4	0	0
923.4	923.4	0	1385.1	461.7	−923.4	461.7	0

combination of right and left circular polarizations, all types of probe and control polarization choices need to be considered into account such as $probe(\pi) - control(\pi)$, $probe(\sigma^+) - control(\sigma^+)$, $probe(\sigma^-) - control(\sigma^-)$, $probe(\pi) - control(\sigma^+)$, $probe(\pi) - control(\sigma^-)$, $probe(\sigma^+) - control(\pi)$, $probe(\sigma^-) - control(\pi)$, $probe(\sigma^+) - control(\sigma^-)$ and $probe(\sigma^-) - control(\sigma^+)$. The Rabi frequencies (Ω_p, Ω_c) are scaled as $\Omega_c \rightarrow s\Omega_c$ and $\Omega_p \rightarrow s'\Omega_p$ when adding contributions where s and s' are the Clebsch-Gordan co-efficients [37] for the respective transitions. However, there is no significant difference in the line shape and positions after considering all possible Λ's within a given case.

As a representative dataset, figure 6 (left) shows all three EIT line shapes riding on the Doppler-broadened absorption profile. Here, the control detuning is set to $\Delta_c = 230.85$ MHz. The corresponding background-subtracted features are zoomed in the insets. The relevant physics is well captured by introducing correct dephasing terms The figures (a,b,c) in figure 6 (Right) show all possible dark resonances with corresponding theoretical model fit. The subplot (c) is the usual single EIT peak, which is also observed in other atoms like Rb, Cs, etc, whereas (d) represents a line shape which is a mixture of dark and bright resonances, appeared at $\Delta_c = -461.7$ MHz. Plots of all line shapes throughout this article are normalized such that the transparency peak is set to 1 and the absorption dip is set to -1. The characteristic variation of EIT line width with Ω_c for the case of $\Delta_c = 0$ MHz is also studied with theoretical fitting. As an example, at $\Delta_c = 0$, EIT features are recorded for case C_1 for various values of control power. The Gaussian background is subtracted and a Lorentzian fit is performed. Figure 7 shows the line width and contrast variation with control Rabi frequency Ω_c. The contrast increases with Ω_c at the expense of broader line width. We also have studied the line-shape characteristics of EIA by varying the

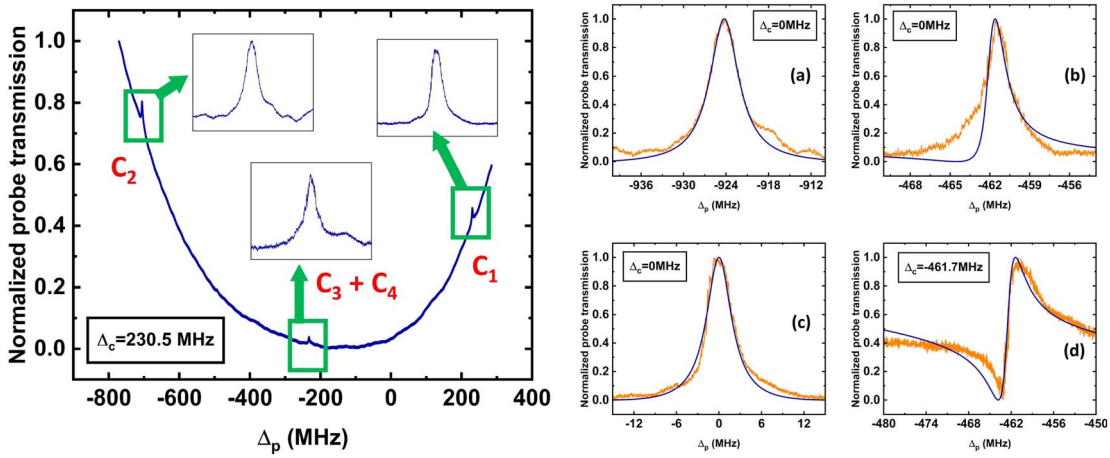

Figure 6. (Left) Observation of three bright resonances for $\Delta_c = 230.85$ MHz. The inset shows the zoomed views. (Right) On-resonant ($\Delta_c = 0$) bright resonance line shapes (a,b,c). The orange line indicates experimental data and the blue line is the theoretical model fit. Subplot (d) shows the admixture of dark and bright resonance at $\Delta_p = -461.7$ MHz.

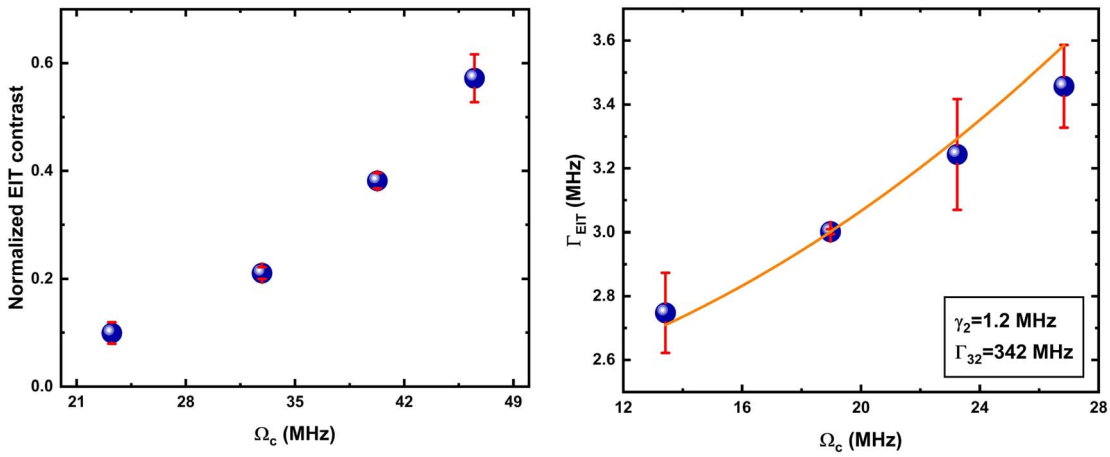

Figure 7. (Left) The variation of EIT contrast with respect to Control Rabi frequency. (Right) The EIT line-width increases with the control beam intensity/Rabi frequency. The blue circles are the data points with error bars indicated in red. The orange line is the fit from the theoretical description.

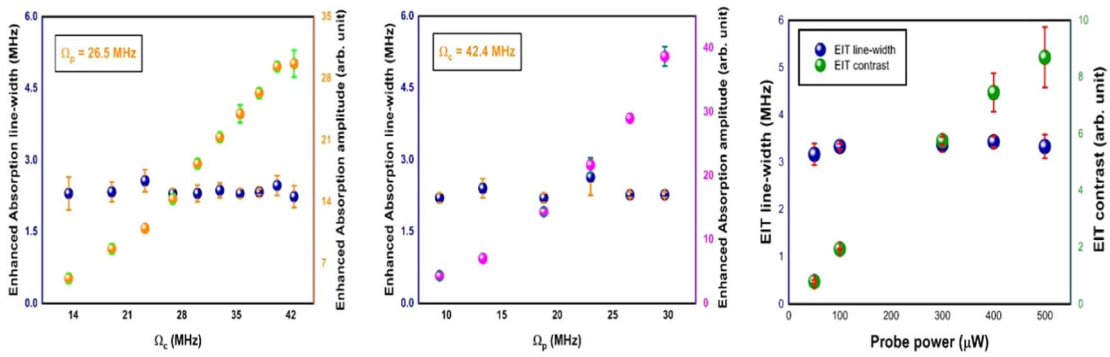

Figure 8. (Left) Enhanced absorption line-width is nearly constant as we varied the control beam Rabi frequency, but the contrast increases. (Middle) The line-width of EIA also remains constant with respect to probe Rabi frequency, but here also the contrast increases. (Right) The EIT line-width is also independent of probe power, but the contrast increases.

control and probe beam intensities. The left and middle sub-figure of figure 8 shows that the EIA or enhanced absorption line-width is nearly constant as we vary probe or control beam intensities at this Rabi frequency ranges. On the other hand, the EIT line-width is also independent of probe power as shown in the right sub-figure of figure 8. In all cases, the contrast increases. By rearranging the imaginary part of probe susceptibility, we can read off the EIT line width [36]

$$\Gamma_{EIT} = 2\left[\gamma_2 + \frac{\Omega_c^2}{\sqrt{OD}\,\Gamma_{32}}\right] \tag{12}$$

where OD is the optical density at a temperature T. The expression for calculating OD [36] is given by

$$OD = \frac{n\omega_p|d_{13}|L}{\epsilon_0 c\hbar\,(\Gamma_{31} + \Gamma_{32})} \tag{13}$$

In the above equation, $n = 2.3 \times 10^{10}$ atoms/c.c. is the atomic density at cell temperature $T = 60°$C, $\omega_p = 2\pi \times 391.016$ THz is the probe frequency in D_2 line, $|d_{13}| = 2.46 \times 10^{-29}$ C-m is the dipole matrix element [24], $L = 75$mm is the cell length, ϵ_0, $\hbar$, c are vacuum permittivity, reduced Planck's constant, velocity of light respectively and Γ_{31},Γ_{32} are Doppler broadened spontaneous decay rates. The density at temperature T is calculated by first calculating the pressure using [24]

$$\log p = 7.4077 - \frac{4453}{T} \tag{14}$$

where $P = nk_BT$ is the density. The inclusion of an overlapping Doppler broadened profile enables us to exchange the excitation pathways of the control and probe by the atoms which give two additional features (sub figures a and b in figure 6 (Right)). The asymmetric mismatch between theory and experiment accounts for non-zero probe detuning and the existence of multiple excited states [38] in ^{39}K. The asymmetry primarily originates from the admixture of the pure dark state and the pure bright state, as can be seen in subplot (d) of figure 6(right) where the dip is observed due to bright resonance and the peak is due to dark resonance. The effect of the non-zero single photon detuning makes the line shapes asymmetric, making it deviate from the perfect Lorentzian line shape. It is in general possible to modify the absorption properties of the medium even when both single photon and two-photon resonance conditions are not perfectly satisfied as also indicated in references [39, 40], albeit with a reduced fidelity. We have taken into account all single photon and two photon resonance conditions in equation (1) through equation (6). These equations are valid even when we swap the role of probe and control. In a way, all observed resonances and line shapes are due to the interplay between single photon and two photon resonances.

When the control beam detuning is taken to far-off red detuned, $\Delta_c = -923.4$ MHz, a complete absorption and complete transmission line shapes are observed at probe detunings $\Delta_p = -923.4$ MHz and $\Delta_p = -1846.8$ MHz respectively. For blue-detuning, $\Delta_c = 1385.1$ MHz, complete absorption, and transmission are seen in $\Delta_p = 461.7$ MHz and $\Delta_p = 1385.1$ MHz respectively as shown in figure 9. For the cases of far-off resonant complete absorption, we have adiabatically eliminated [41] state $|F'\rangle$ from the Master equation to obtain the correct line shape by switching off the spontaneous decay in the Lindblad term. This is a reasonable description because—at the far-off resonance from the one-photon transition the lasers do not significantly populate the excited state thereby reducing the spontaneous decay from the excited state. The theoretical model fit gives effective γ_2 values ranging from 1.2 MHz to 2.5 MHz depending on the line shape position. Other variable parameters γ_3, Γ_{31}, Γ_{32} are adjusted according to the probe and control detunings. For a given line shape, if it appears inside the Doppler, then the dephasing will be controlled by the spontaneous decay term. If it appears outside the Doppler, then the dephasing will come primarily from γ_3. As an example, for $\Delta_c = -923.4$ MHz (case C_3), the values of $\gamma_2 = 1.2$ MHz, $\Gamma_{31} = \Gamma_{32} = 0$ and $\gamma_3 = 342$ MHz. Figure 10 (right a-i) shows a transition from bright resonance to dark resonance as we vary the control beam detuning while maintaining the probe laser scanning across the entire D_2 manifold. The blue side of this case always yields a dark resonance as can be seen from (f-i) of figure 10(right). Line-plot colors are chosen to represent the detuning of the control beam. These line shapes are obtained for Case C_1. A similar transition can also be observed in other cases. To indicate the extent of mixing of bright and dark resonances, the ad-mixing parameter η is defined as the ratio of the bright resonance contrast (defined as b) to the dark resonance contrast (defined as d). The variation in η is plotted against the control beam detuning which gave an exponential crossover from bright resonance to dark resonance as we sweep the control beam detuning as shown in figure 11. The value of the admixture parameter η is specific to the experimental details such as the detector used, gain, and offset of the detector. However, the η vs Δ_c plots essentially capture the gradual decline in adiabatic elimination as the control beam is swept from the red side to the blue side for a particular line shape. The admixture parameter plot will help determine whether the line shape is formed in standard configuration C_1 or in the swapped frame configuration C_2. Figure 11 shows the case for C_1 whereas, for C_2, the admixture parameter η is maximum at the blue side and gradually approaches

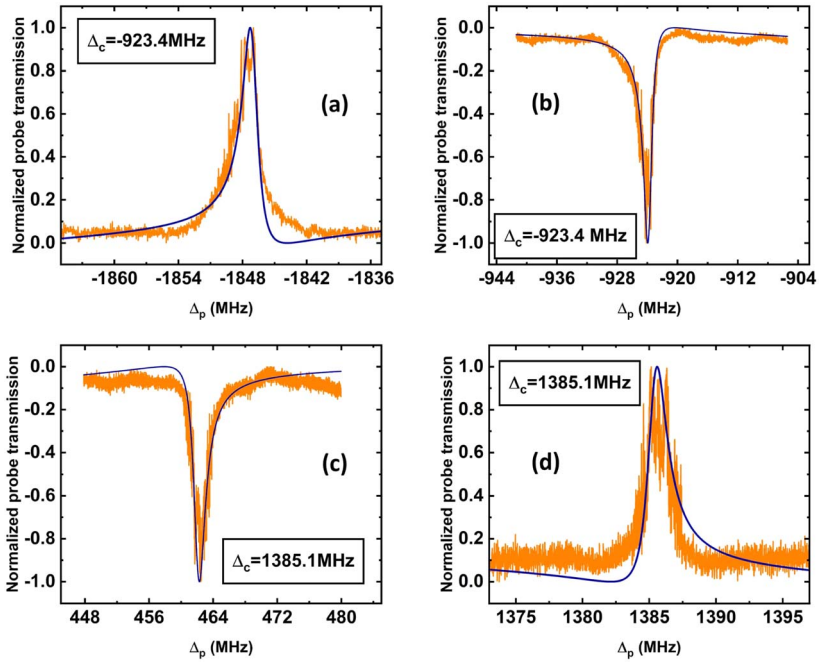

Figure 9. (a) EIT as C_2 feature at $\Delta_c = -923.4$ MHz. (b) EIA as C_1 feature at $\Delta_c = -923.4$ MHZ. (c) EIA as C_2 feature at $\Delta_c = 1385.1$ MHz. (d) EIT as C_1 feature at $\Delta_c = 1385.1$ MHZ.

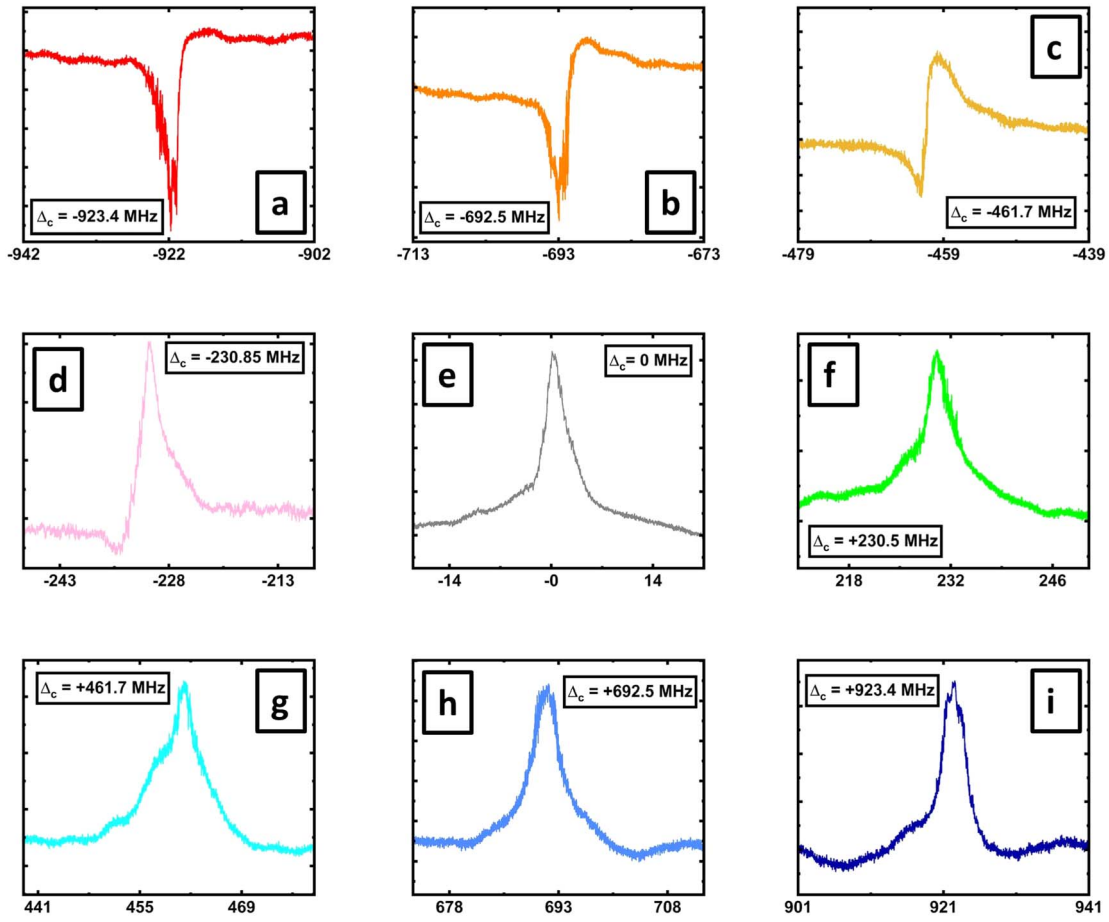

Figure 10. Group of subplots indicating the crossover from complete absorption to complete transparency shown for the feature C_1. The control beam detuning Δ_c is varied from red detuning $\Delta_c = -923.4$ MHz to blue detuning $\Delta_c = 923.4$ MHz.

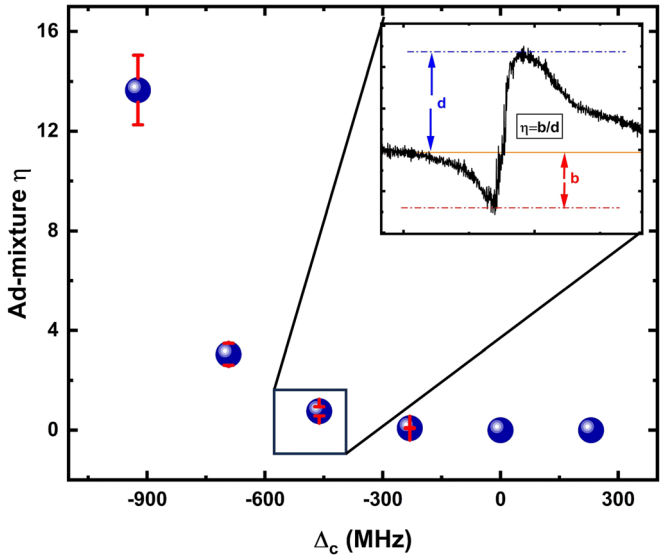

Figure 11. Ad-mixture parameter η as a function of control detuning Δ_c. As Δ_c is swept from the red side to the blue side, complete transparency is obtained due to the formation of dark resonance, consequently, the bright state ad-mixture parameter η vanishes after $\Delta_c \geqslant 0$.

zero near resonance, similar to C_1. This indicates that near resonance, the probability of observing a dark resonance is high in all cases. As detuning increases or decreases, the admixture plays a crucial role through adiabatic elimination.

5. Conclusion and outlook

By choosing both the Doppler and exchanging the probe and control beam excitation routes, we have been able to explain all possible line shapes and positions, which matched well with the density matrix formalism-based theoretical model. Adiabatic elimination works well to describe the bright resonance in the blue and red detuning regions. The exact line shape can be matched by considering the intervention of other excited states [29]. To the best of our knowledge, these observations of additional resonances and a smooth crossover from EIT to EIA have not been reported in previous EIT-EIA studies. These unique results in ^{39}K are obtained primarily because the Doppler broadening is comparable to ground hyperfine splitting, - which is not readily available in other experimental systems typically used for EIT-EIA studies.

Beyond the Gaussian probe and control, a probe beam carrying orbital angular momentum (Laguerre–Gaussian mode) can have a fundamentally unique response [42, 43] to this EIT medium because of the spatial variation of Rabi frequency that can lead to line shape narrowing [44] as well as change in asymmetries. A novel direction to explore EIT in Potassium is to study cold Potassium atoms [45] in a strong magnetic field where the external magnetic field can couple the Zeeman sub-levels of different hyperfine states. Another interesting avenue in quantum optics with atoms in magnetic field is to explore the non-reciprocity. A very recent trend is to explore non-magnetic non-reciprocity, for e.g. in [46] EIT with atoms in a ring cavity system is used to generate the chiral response from atoms while [47] investigates relative motion of NV centres with respect to co and counter propagating beams to study non-reciprocity. The phenomenon of non-reciprocity has several applications such as optical isolators, circulators, optical device making. As an outlook, we intend to explore non-reciprocity in quantum interference in ^{39}K in presence of magnetic field. The explanation of all these quantum interference line shapes enriches the understanding of quantum coherence and has applications in frequency-offset tight laser locking [48] and quantum technology applications such as optical isolators, [49] quantum memory [8], and slow light [9]. Generally, our technique can be extended to any system including artificial atoms [50, 51].

Acknowledgments

The authors thank Dr. Sanjukta Roy for insightful discussions. The authors also thank S Majumder and A Misra for their discussions and assistance. The authors also thank the RRI IT section and workshop. The authors

acknowledge funding support from the Department of Science and Technology (DST), Govt of India, and I-HUB Quantum Technology Foundation through grant number I-HUB/SPIKE/2023-24/004.

Data availability statement

The data cannot be made publicly available upon publication because they are not available in a format that is sufficiently accessible or reusable by other researchers. The data that support the findings of this study are available upon reasonable request from the authors.

Funding

The funding for this research has been provided by the Department of Science and Technology (DST), Govt. of India and I-HUB Quantum Technology Foundation through grant number I-HUB/SPIKE/2023-24/004.

Conflict of interest statement

The authors declare that no competing interests exist

ORCID iDs

Gourab Pal https://orcid.org/0000-0002-6595-5436
Subhasish Dutta Gupta https://orcid.org/0000-0002-7168-8549
Saptarishi Chaudhuri https://orcid.org/0000-0001-5069-6307

References

[1] Fleischhauer M, Imamoglu A and Marangos J P 2005 *Rev. Mod. Phys.* **77** 633–73
[2] Finkelstein R, Bali S, Firstenberg O and Novikova I 2023 *New J. Phys.* **25** 035001
[3] Novikova I, Walsworth R and Xiao Y 2012 *Laser Photonics Rev.* **6** 333–53
[4] Yang X, Zhou Y and Xiao M 2013 *Sci. Rep.* **3** 3479
[5] Kitching J 2018 *Applied Physics Reviews* **5** 031302
[6] Ludlow A D, Boyd M M, Ye J, Peik E and Schmidt P O 2015 *Rev. Mod. Phys.* **87** 637–701
[7] Li J, Quan W, Zhou B, Wang Z, Lu J, Hu Z, Liu G and Fang J 2018 *IEEE Sensors J.* **18** 8198–207
[8] Ma L, Slattery O and Tang X 2017 *J. Opt.* **19** 043001
[9] Jen H H, Xiong B, Yu I A and Wang D W 2013 *J. Opt. Soc. Am.* B **30** 2855–63
[10] Hain M, Stabel M and Halfmann T 2022 *New J. Phys.* **24** 023012
[11] Doai L V, Khoa D X and Bang N H 2015 *Phys. Scr.* **90** 045502
[12] Shu C, Chen P, Chow T K A, Zhu L, Xiao Y, Loy M M T and Du S 2016 *Nat. Commun.* **7** 12783
[13] Soni J, Mansha S, Gupta S D, Banerjee A and Ghosh N 2014 *Opt. Lett.* **39** 4100–3
[14] Zhang X J, Wang H H, Liang Z P, Xu Y, Fan C B, Liu C Z and Gao J Y 2015 *Phys. Rev.* A **91** 033831
[15] Das C, Dey S and Ray B 2022 *Phys. Scr.* **97** 095401
[16] Sargsyan A, Leroy C, Pashayan-Leroy Y, Sarkisyan D, Slavov D and Cartaleva S 2012 *Opt. Commun.* **285** 2090–5
[17] Hussain B, Khan S N, Ilyas M, Anwar M and Ikram M 2024 *Phys. Scr.* **99** 055113
[18] Yoshida I, Hayashi N, Fujita K, Taniguchi S, Hoshina Y and Mitsunaga M 2013 *Phys. Rev.* A **87** 023836
[19] Maynard M A, Bouchez R, Lugani J, Bretenaker F, Goldfarb F and Brion E 2015 *Phys. Rev.* A **92** 053803
[20] Neveu P, Banerjee C, Lugani J, Bretenaker F, Brion E and Goldfarb F 2018 *New J. Phys.* **20** 083043
[21] Wu M, Bao X, Yu S, Yi L, Ren P, Deng S and Wu H 2023 Electromagnetically Induced Transparency Spectra of 6Li Rydberg Atoms *Photonics* **10** 1367
[22] Cheng H, Wang H M, Zhang S S, Xin P P, Luo J and Liu H P 2017 *Opt. Express* **25** 33575–87
[23] Barik S S B, Chaudhuri S K and Roy S 2022 *Opt. Continuum* **1** 1176–92
[24] Tiecke T G 2011 Properties of potassium *Semantic Scholar* **35609312** 1–14 https://api.semanticscholar.org/CorpusID:35609312
[25] Long D A, Fleisher A J, Plusquellic D F and Hodges J T 2017 *Opt. Lett.* **42** 4430–3
[26] Sargsyan A, Petrov P A, Vartanyan T A and Sarkisyan D 2016 *Opt. Spectrosc.* **120** 339–44
[27] Gozzini S, Fioretti A, Lucchesini A, Marmugi L, Marinelli C, Tsvetkov S, Gateva S and Cartaleva S 2017 *Opt. Lett.* **42** 2930–3
[28] Taskova E, Alipieva E, Andreeva C and Brazhnikov D 2020 *J. Phys. Conf. Ser.* **1492** 012011
[29] Subba I H, Singh R K, Sharma N, Chatterjee S and Tripathi A 2020 *Eur. Phys. J.* D **74** 136
[30] Khoa D X, Trung L C, Thuan P V, Doai L V and Bang N H 2017 *J. Opt. Soc. Am.* B **34** 1255–63
[31] Wang J 2010 *Phys. Rev.* A **81** 033841
[32] Wang B X, Tao M J, Ai Q, Xin T, Lambert N, Ruan D, Cheng Y C, Nori F, Deng F G and Long G L 2018 *npj Quantum Information* **4** 52
[33] Ishizaki A and Fleming G R 2009 *Proc. Natl Acad. Sci.* **106** 17255–60
[34] Laskar R, Hossain M M and Saha J K 2021 *Phys. Scr.* **96** 035108
[35] Mondal S and Bandyopadhyay A 2023 *Phys. Scr.* **98** 115508
[36] DeRose K, Jiang K, Li J, Julius M, Zhuo L, Wenner S and Bali S 2023 *Am. J. Phys.* **91** 193–205
[37] 2023 Rubidium 87 d line data Online available at https://steck.us/alkalidata/rubidium87numbers.pdf.
[38] Chen Z R and Su X M 2013 *Eur. Phys. J.* D **67** 138

[39] Wang Y Y, Qiu J, Chu Y Q, Zhang M, Cai J, Ai Q and Deng F G 2018 *Phys. Rev.* A **97** 042313
[40] Dong H, Xu D Z, Huang J F and Sun C P 2012 *Light: Science & Applications* **1** e2–2
[41] Brion E, Pedersen L H and Mølmer K 2007 *J. Phys. A: Math. Theor.* **40** 1033
[42] Wang Y, Guo M, Wu J, Liu J, Yang X and Li J 2022 *Opt. Express* **30** 43426–38
[43] Manchaiah D, Kumar R and Easwaran R K 2023 *New J. Phys.* **25** 013013
[44] Das B C, Bhattacharyya D and De S 2016 *Chem. Phys. Lett.* **644** 212–8
[45] Sutradhar S, Misra A, Pal G, Majumder S, Roy S and Chaudhuri S 2023 *AIP Adv.* **13** 065317
[46] Zhang S, Hu Y, Lin G, Niu Y, Xia K, Gong J and Gong S 2018 *Nat. Photonics* **12** 744–8
[47] Huang H B, Lin J J, Yao Y X, Xia K Y, Yin Z Q and Ai Q 2022 *Ann. Phys.* **534** 2200157
[48] Ying K, Niu Y, Chen D, Cai H, Qu R and Gong S 2014 *Appl. Opt.* **53** 2632–7
[49] Weller L, Kleinbach K S, Zentile M A, Knappe S, Hughes I G and Adams C S 2012 *Opt. Lett.* **37** 3405–7
[50] Chang Y H, Dubyna D, Chien W C, Chen C H, Wu C S and Kuo W 2022 *Sci. Rep.* **12** 22308
[51] Kannan B *et al* 2020 *Nature* **583** 775–9